



Cite this: *Nanoscale*, 2018, **10**, 12378

Reconstructing a plasmonic metasurface for a broadband high-efficiency optical vortex in the visible frequency

Bing-Rui Lu,^a Jianan Deng,^a Qi Li,^b Sichao Zhang,^a Jing Zhou,^c Lei Zhou^{*b} and Yifang Chen^{*a}

Metasurfaces consisting of a two-dimensional metallic nano-antenna array are capable of transferring a Gaussian beam into an optical vortex with a helical phase front and a phase singularity by manipulating the polarization/phase status of light. This miniaturizes a laboratory scaled optical system into a wafer scale component, opening up a new area for broad applications in optics. However, the low conversion efficiency to generate a vortex beam from circularly polarized light hinders further development. This paper reports our recent success in improving the efficiency over a broad waveband at the visible frequency compared with the existing work. The choice of material, the geometry and the spatial organization of meta-atoms, and the fabrication fidelity are theoretically investigated by the Jones matrix method. The theoretical conversion efficiency over 40% in the visible wavelength range is worked out by systematic calculation using the finite difference time domain (FDTD) method. The fabricated metasurface based on the parameters by theoretical optimization demonstrates a high quality vortex in optical frequencies with a significantly enhanced efficiency of over 20% in a broad waveband.

Received 13th March 2018,

Accepted 16th May 2018

DOI: 10.1039/c8nr02088d

rsc.li/nanoscale

Introduction

An optical vortex has a helical phase front and a phase singularity.¹ It can be transformed from a Gaussian beam through manipulations of the polarization/phase status of light.^{2,3} In this process, the spin angular momentum (SAM) of the photon is converted to the orbital angular momentum (OAM) to form a vortex beam. In normal light with a Gaussian distribution of intensity, there are only two spin states of the photon, namely $S^z = \pm\hbar$, with \hbar as the reduced Planck constant, z as the beam axis and the sign determined by the handedness of the circular polarization of the beam. When the Gaussian beam is converted into a donut shape, the density of states (DOE) of a photon is dramatically increased because the OAM per photon is expressed as unbounded $L^z = l\hbar$ where l can be any positive or negative integer.^{4,5} Communication using light with a vortex wave-front is able to transmit a tremendously larger amount of information than the normal light.^{6–8} Apart from this, with the

unique quantum characteristics⁹ and mechanical actions on small particles,¹⁰ an optical vortex also has high prospects of broad applications¹¹ in quantum based optics,^{12,13} computation,^{14,15} optical microscopy,^{16,17} optical tweezers^{18,19} and astronomical filters.^{20,21}

Such vortex beams are traditionally realized through discrete optical components such as spiral phase plates,^{22,23} axicon lenses,^{1,24} dove prisms,^{25,26} computer generated holograms,^{27,28} space-variant birefringent retarders²⁹ and even other interferometer setups,^{30,31} which are typically bulky and macroscopic.³²

An alternative is to employ metasurface, which are constructed from nano-metallic structures organized in specific orientations with subwavelength distances from each other. With a subwavelength thickness, metasurfaces are able to miniaturize a lab-scale optical system into a chip-scale component through optical integration, attracting worldwide attention for developing a new generation of optical devices with extraordinary functionalities.³²

Due to the impedance of metallic structures, metasurface based devices suffer from low conversion efficiency in light manipulation^{33–39} since the majority of the energy is lost by scattering or Joule loss in metals, hindering practical applications. So far, substantial attempts have been made to enhance the efficiency by optimizing the metasurface structure such as employing metal–insulator–metal (MIM) stacks^{40,41} and dielectric materials^{33,37,42} with a high refractive index. A high conversion efficiency of over 90% in reflection mode³³

^aNanolithography and Application Research Group, State Key Lab of ASIC and System, School of Information Science and Engineering, Fudan University, Shanghai 200433, P. R. China. E-mail: yifangchen@fudan.edu.cn

^bState Key Laboratory of Surface Physics and Key Laboratory of Micro and Nano Photonic Structures (Ministry of Education), Fudan University, Shanghai 200433, P. R. China. E-mail: phzhou@fudan.edu.cn

^cState Key Laboratory of Infrared Physics, Shanghai Institute of Technical Physics, Chinese Academy of Sciences, 500 Yutian Road, Shanghai 200083, China

and ~50% in transmission mode³⁵ has been reported with metasurfaces in the infrared or longer wavelength range.

On the other hand, a relatively higher efficiency has only been achieved in a narrow waveband at visible wavelengths,^{38,40,43} by metasurfaces constructed from metals^{5,36,38,43–45} and MIM stacks.^{40,41} Au^{5,36,40,41,43–46} and Ag^{33,38} are two commonly used metals in fabricating metasurfaces due to their excellent plasmonic properties. There have been reports applying dielectric materials with less loss than metals for constructing metasurfaces.^{47–49} In order to achieve similar performances, however, dielectric metasurfaces typically require high-aspect-ratio nano-structures because of the relatively lower refractive index of the material,^{37,42} which calls for complex nanofabrication processes such as electron beam lithography (EBL), atomic layer deposition (ALD) and reactive ion etching (RIE).⁴²

As is well known, the conversion efficiency is highly related to the material nature, the geometry and the spatial organization of the elements forming the metasurface, yet the choice of material is an important degree of freedom that is often overlooked in improving the performance of metasurfaces. In this work, it was found that rather than Au and Ag as the metasurface materials, Al can be an even better choice for a much wider waveband range in the visible frequency. Moreover, besides the geometry and spatial organization of the meta-atoms, a delicate architecture by state-of-the-art nanofabrication is essential for successfully achieving the designed nano-antennas. This letter reports our systematic study of how to significantly enhance the SAM–OAM conversion efficiency in a broadband of visible light well beyond the reported figures^{5,44} by reconstructing a plasmonic metasurface with L-shaped elements.

Theoretical calculation and simulations

As illustrated in Fig. 1(a), the metasurface concerned in this study consists of metallic L-shaped elements arranged in con-

centric circles on a quartz substrate.^{5,50} The L-shape design is a two-oscillator element which provides better structural anisotropic properties compared to a single-arm antenna.^{50,51} The metasurface reverses the circular polarization direction of a perpendicularly incident light. The flip of the spin angular momentum generates the orbital angular momentum of the photons for the momentum conservation. In order to maximize the Spin-to-Orbit Conversion (SOC) efficiency, the shape of the antennas on the metasurface is optimized by studying the phase retardation of the structure, while the arrangement and the thickness were systematically compared using theoretical calculation combined with the FDTD method in the investigation.

The two arms of the L-shaped antenna are identical in size at a right angle. The width and length of the arms are 55 nm and 210 nm, respectively, as shown in Fig. 1(b). It also depicts that along each completed ring path the antennas rotate a full circle with a constant spacing in between. The rotation of each antenna can be described with the following orientation of the transferred axis,

$$\alpha(\rho, \theta) = q\theta + \alpha_0, \quad (1)$$

where (ρ, θ) is the polar coordinate of the nano-antenna with $(0, 0)$ being the center of the metasurface, α_0 is a constant reference angle to describe the initial orientation of the antenna when $\theta = 0$, and q is a constant to describe the number of rotation circles along a completed path of each ring. In our design, $\alpha_0 = \pi/4$ and $q = 1$.

Based on the Pancharatnam–Berry phase mechanism, the α degree rotation of the nano-antenna leads to a 2α geometric phase shift in the output. Hence, the topological charge of the wave is defined by the magnitude of the nano-antenna rotations. For $q = 1/2$, the antenna rotates a half-circle and the transformed light achieves a full range of phase shift from $-\pi$ to π , carrying OAM with a topological charge of $l = \pm 2q = \pm 1$, with the sign determined by the handedness of the circular polarization. In our design with $q = 1$, the elements rotate a full circle and the yielded light carries a topological charge of $l = \pm 2$ with two full-range phase shifts. Fig. 1(c) describes the

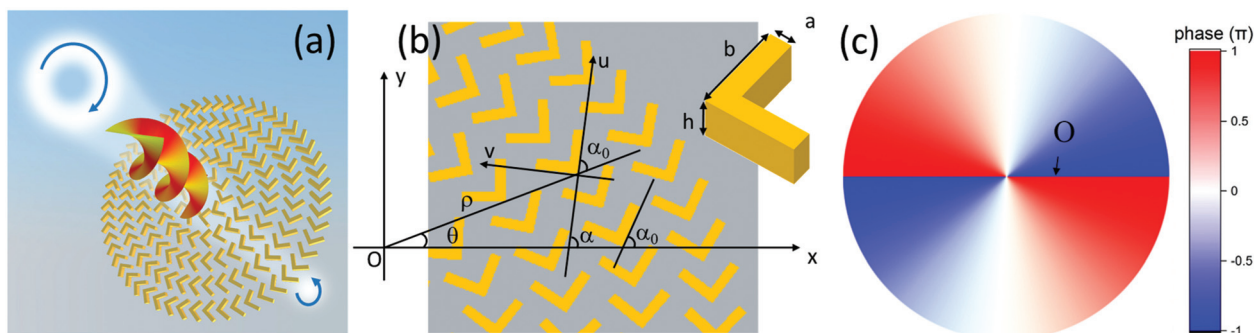


Fig. 1 (a) An incident Gaussian beam of light with left circular polarization passes through the plasmonic metasurface, transforming into a right circular polarized vortex beam with a spiral wave front and a donut shape of the intensity. (b) The nano-antenna with the polar coordinate of (ρ, θ) has a rotation of $q\theta + \alpha_0$. The two arms of the L-shaped antenna are of the same size with the width a of 50 nm and length of 210 nm. The thickness of the antenna is a parameter to be discussed later to optimize the conversion efficiency. (c) The simulated phase distribution on a transverse plane of the transformed light at the wavelength of 618 nm with the phase singularity at the center O.

simulated phase distribution on a transverse plane of the transformed light at the wavelength of 618 nm with the phase singularity at the centre O.

In order to theoretically calculate the efficiency of the designed metasurface with the L-shaped structural configuration, two Jones matrices $\mathbf{T}(0) = \begin{pmatrix} t_{uu} & t_{uv} \\ t_{vu} & t_{vv} \end{pmatrix}$ and $\mathbf{R}(0) = \begin{pmatrix} r_{uu} & r_{uv} \\ r_{vu} & r_{vv} \end{pmatrix}$ are used to describe the transmission and reflection properties of the structure,^{52,53} where u and v are two orthogonal local coordinate axes. With a circularly polarized input mode and the unit cells rotated by an angle θ , the abnormal transmission of the structure can be described as $T_a^r = T_a/(T_a + T_n + R_a + R_n)$, where T_a , T_n and R_a , R_n are the absolute rate of the abnormal and normal transmission/reflection modes in the output:

$$\begin{aligned} T_a &= \left| \frac{1}{2}(t_{uu} - t_{vv}) \pm \frac{i}{2}(t_{uv} + t_{vu}) \right|^2 \\ T_n &= \left| \frac{1}{2}(t_{uu} + t_{vv}) \pm \frac{i}{2}(t_{uv} - t_{vu}) \right|^2 \\ R_a &= \left| \frac{1}{2}(r_{uu} - r_{vv}) \pm \frac{i}{2}(r_{uv} + r_{vu}) \right|^2 \\ R_n &= \left| \frac{1}{2}(r_{uu} + r_{vv}) \pm \frac{i}{2}(r_{uv} - r_{vu}) \right|^2. \end{aligned} \quad (2)$$

Therefore, once the Jones-matrix elements of the designed meta-atom (typically being periodically repeated to form an array) are obtained by numerical simulations, the efficiency of a meta-device (say, the vortex generator studied here) constructed by such a meta-atom can be readily calculated by eqn (2). It is important to stress that the rotation of the nano-antenna along the circular path of the metasurface has an effect on the phase but not the momentum conversion of the photons. It is the two arms of the nano-antenna that offer a wavelength-dependent birefringent phase retardation δ between the two linearly orthogonal polarization states, which is the fundamental cause to induce the OAM and predo-

minantly affects the efficiency (eqn (2)). Assuming that the transmission amplitudes for waves polarized along two principal axes do not exhibit a large difference, when δ has an optimal tuning of π , the handedness of the output circular polarization is completely inverted. When $\delta \neq \pi$, it would result in a superposition of the transformed and untransformed waves, among which the percentage of the transformed wave determines the SOC efficiency of the plasmonic metasurface.

With the abovementioned theory as the foundation of this work to discuss the conversion efficiency $T_a^r = T_a/(T_a + T_n)$, the circular arrangement of the nano-antenna array can be simplified to a square array⁵ with the periods p_u and p_v on the u - and v -axes during the FDTD simulation to optimize the antenna material and geometric parameters such as the period and thickness for an enhanced SOC efficiency. Fig. 2(a) shows the calculated birefringent phase retardation at the wavelengths of 400–900 nm for Al antennas arranged in a square array with $p_u = p_v = 350$ nm.

For choosing the material for the nano-antennas of plasmonic metasurfaces, a comparison between the materials is carried out with the simplified array of the designed metasurface. Although Ag and Au are frequently chosen because of their low absorption, the strong plasmonic properties of Al would compensate for the absorption problem, making it a better choice for our design. In the FDTD simulation in Fig. 2(b), the structural configuration of the antenna has a thickness of 60 nm and a period of $p_u = 200$ nm and $p_v = 350$ nm. The results show that Al shows the best performance among Al, Au, Ag and Si in the visible regime, covering the broadest wavelength range with a high conversion efficiency. For an unknown material with a dielectric coefficient of $\epsilon = \epsilon_1 + i\epsilon_2$, an increase in the absorption can lead to a decline in the conversion efficiency, while the increased anisotropic property of the material will have the opposite effect on the conversion efficiency. Compared to the counterparts of Ag and Au, the dispersions of Al in the visible frequency in Fig. 2(c) represent a stronger anisotropic property at higher frequencies, leading to

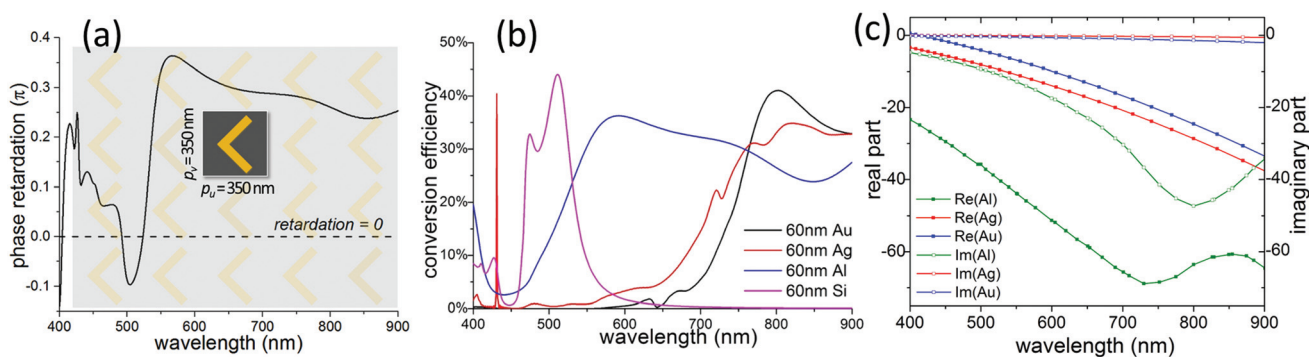


Fig. 2 (a) The calculated birefringent phase retardation at wavelengths of 400–900 nm of a squarely arranged nano-antenna array with $p_u = p_v = 350$ nm. (b) The comparison between different materials Au, Ag, Al and Si for the nano-antennas with $p_u = 200$ nm and $p_v = 350$ nm. (c) The dispersions of Al, Ag and Au in the visible wavelength range, which demonstrates that Al has stronger anisotropic property than Ag and Au over the full bandwidth and an increased absorption at the wavelength of ~ 800 nm.

an increased conversion efficiency, while the increased absorption lowers the efficiency at the wavelength of ~ 800 nm in Fig. 2(b).

The effect of the period p_u on the metasurface conversion efficiency for the range from 1000 nm to 100 nm was systematically studied by numerical simulation in this work. When p_u is larger than the wavelength, each nano-antenna behaves as an *independent* element for momentum conversion. Increasing the density of the antennas in the square array is beneficial to enhance the conversion efficiency. On the other hand, in the subwavelength regime, the reduction of p_u may strengthen the coupling between the closely spaced antennas, which not only brings down the resonance Q factor but also increases the complexity of the fabrication process. For example, Fig. 3(a)–(c) compare the conversion efficiency dependence on the wavelength and the near-field $|E|$ distributions of the L-shaped antennas when p_v is 350 nm and p_u changes from 1000 nm down to 200 nm, respectively. In Fig. 3(a), when p_u is 1000 nm the near-field $|E|$ distribution shows only the local resonance with negligible coupling between the neighboring antennas. The resonance within each antenna is the dominant

factor in the conversion efficiency. An increase of the unit density, corresponding to the pitch reduction from 1000 nm (Fig. 3(c-1)) down to 200 nm (Fig. 3(c-2)), dramatically increases the efficiency. Fig. 3(b) theoretically demonstrates that the stronger coupling between antennas ($p_u = 200$ nm) can bring down the efficiency. At the wavelength of 550 nm, the coupling between antennas is relatively weak, giving rise to an efficiency higher than that at 466 nm which suffers from relatively strong coupling. Therefore, it is necessary to figure out the optimized antenna pitch p_u to maximize the conversion efficiency in constructing the metasurface. The period of 350 nm for p_v and 200 nm for p_u , respectively, to satisfy both the subwavelength conditions and the high quality fabrication is then worked out through our systematic simulation as well as a processing study, which will be discussed later.

Fig. 3(d) and (e) present the overview of the efficiency in both the p_u -wavelength plane and the Al thickness-wavelength plane, generated by FDTD simulation for the nano-antenna arrays with p_u fixed at 350 nm as limited by the geometry size of each antenna. The dashed line in Fig. 3(d) defines the border between two areas with and without the subwavelength

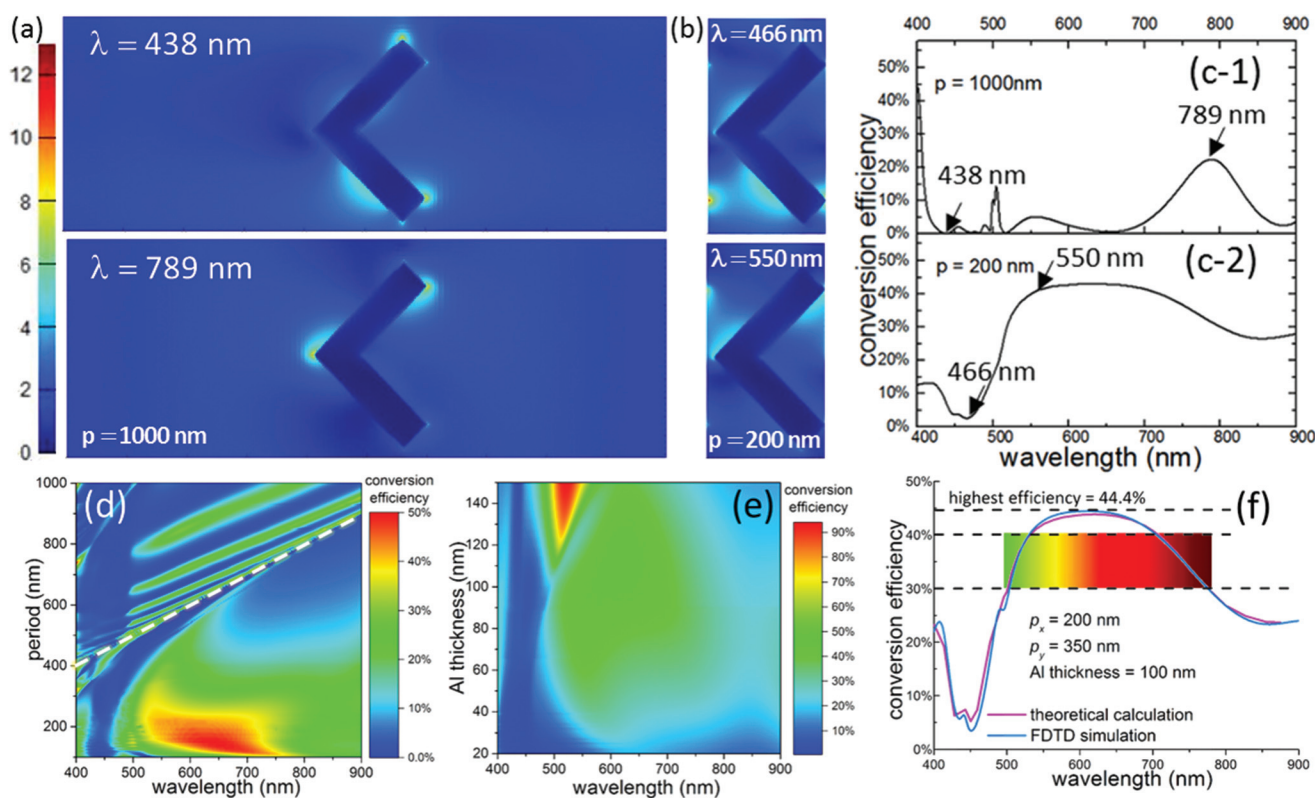


Fig. 3 Geometric optimization study by the FDTD method for the period of the nano-antenna array and the Al thickness of each element to achieve the highest conversion efficiency at visible wavelengths. The near-field $|E|$ distributions of the nano-antenna at different wavelengths when the period on the u -axis is (a) 1000 nm and (b) 200 nm, and (c) their simulated conversion efficiency for the wavelengths from 400 nm to 900 nm demonstrate the correlation between the inter-unit coupling and the SOC efficiency. The lower inter-unit coupling results in higher conversion efficiency. (d) For the period from 100 nm to 1000 nm, the maximum conversion efficiency can be obtained when it is around 200 nm. The dotted line marks when the period equals the wavelength. Below the dotted line is the subwavelength periodic structural configuration. (e) For the Al thickness from 20 nm to 150 nm, the peak conversion efficiency is obtained when it is around 100 nm. (f) The SOC efficiency for the metasurface with the antenna period of 200 nm and the thickness of 100 nm achieves a high efficiency of $>40\%$ at the wavelengths of 548–725 nm. The theoretical calculation using Jones matrices shows high consistency with the FDTD simulation results.

nature, respectively. Clearly, the p_u of 200 nm gives rise to the highest efficiency in the broadest wavelength range.

Similarly, in Fig. 3(e) the efficiencies of the metasurface with the Al layer thickness ranging from 20 to 150 nm are also simulated with the optimized p_u and p_v . Fig. 3(f) shows the efficiency spectrum for the Al thickness of 100 nm. The theoretical calculation results are highly consistent with the FDTD simulated ones. A broad wavelength range of 518–805 nm is achieved in which the conversion efficiency is over 30%, reaches 40% at the wavelength of 548–725 nm and peaks to 43% at the wavelength of 594–674 nm. This improves the efficiency demonstrated by similar structures of metasurfaces made from Au with larger periods.⁵

Experimental details and measurements

It is hard to generate sharp corners in antenna arms using nanofabrication by EBL because of the proximity effect.⁵⁴ The level of discrepancy between the fabricated and the simulated SOC efficiency is strongly affected by the fidelity of the fabricated metasurface elements to the design. Fig. 4 shows how the structural distortion influences sensitively the conversion efficiency (Fig. 4(a) and (b)), the phase retardation and the near-field $|E|$ distribution at the wavelength of 700 nm (Fig. 4(c)). Even though the near field $|E|$ distribution stays almost the same, there is a dramatic phase retardation difference when the discrepancy in the antenna shape happens. This causes the conversion efficiency to change accordingly, leaving a much smaller window of the high efficiency conversion. As a result, it is of significant importance to ensure the fidelity of the antenna structure during the fabrication.

To ensure that the fabricated L-shape antennas faithfully follow the modeled structure, careful EBL proximity effect correction (PEC) to apply different exposure dosages and pattern proximity correction (PPC) to alter the local structural detail of the design for a desired exposure shape are applied to achieve uniform exposure of the resist by the e-beam over the designed

L-shape patterns. The L-shaped nano-antennas of Al with a 350 nm period in the radial direction and a 200 nm period along the ring path are fabricated on a quartz substrate by high resolution EBL using a JEOL-6300FS beam-writer. To ensure a successful lift-off for the 100 nm-thick Al structures, a bilayer of PMMA(MW 100k)/PMMA(MW 350k) is applied to create an undercut profile in the resist after exposure and development.⁵⁴ The PMMA resists are consecutively spin coated on quartz and oven baked at 180 °C for 1 hour. A conductive coating of SX AR-PC 5000/90.2 by Allresist GmbH is then applied to facilitate the discharge during e-beam exposure. Micrographs obtained using a high resolution (2 nm) scanning electron microscope (SEM), Zeiss Sigma HD, in Fig. 5(a), show lithographically defined nano-antenna structures in PMMA. The pattern is then transferred into the Al layer to form the desired antennas by thermal deposition of 100 nm thick Al, followed by a lift-off process with the results shown in Fig. 5(b). Both the arm width uniformity and the corner sharpness of the fabricated elements are the key to ensure that the measured conversion efficiency is as close as possible to the theoretical figure.

An optical setup as schematically depicted in Fig. 6(a) is used to observe the transformed vortex beam by the fabricated L-shaped metasurface with laser sources at 532 nm and 638 nm. An incident light with a plane wave propagates

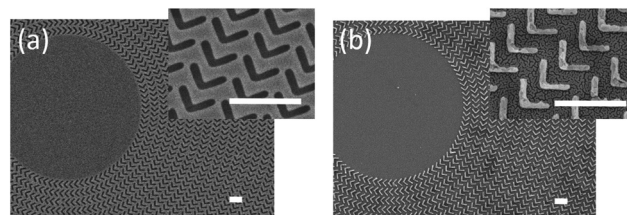


Fig. 5 (a) The SEM picture of the EBL defined L shaped nano-antennas on the quartz substrate in a bi-layer PMMA resist with molecular weights of 350k and 100k, the application of the PEC and PPC ensures the precise definition of the lines and jogs. (b) The Al plasmonic nano-antenna array after the thermal metal deposition and lift-off process. The scale bars in all the SEM pictures are 500 nm.

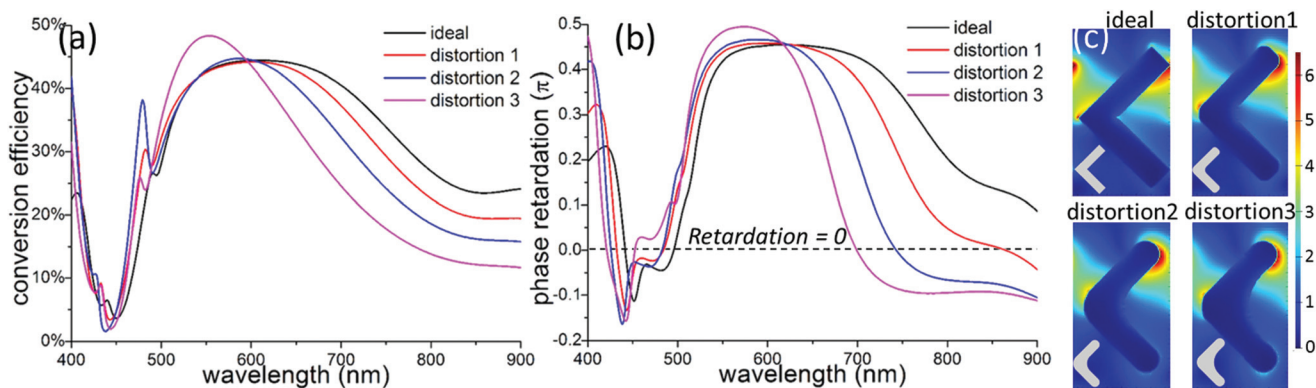


Fig. 4 The comparison between the designed structure and the three possible distortions that might occur during fabrication on (a) the conversion efficiency and (b) the phase retardation in the visible wavelength range, and the near-field $|E|$ distribution at the wavelength of 700 nm.

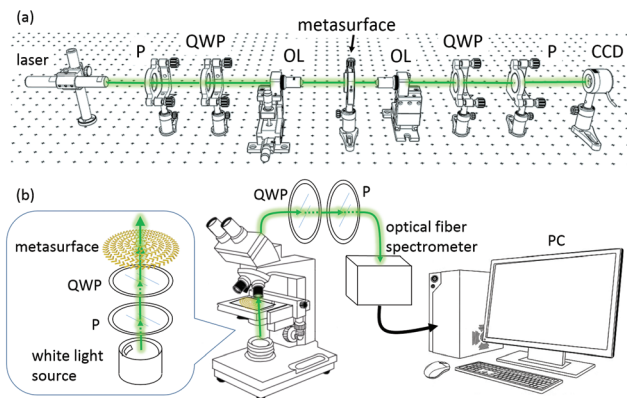


Fig. 6 The optical setup for the optical vortex measurements. (a) The setup with the laser source for a single wavelength measurement. (b) The setup with a white light source to measure the conversion efficiency in the visible range using an optical fiber spectrometer. P: polarizer, QWP: quarter wave plate, OL: optical lens, CCD: charge-coupled device camera.

through a polarizer and a quarter wave plate, being transformed into circularly polarized, and then shines perpendicularly to the metasurface. The metasurface flips a portion of the photons' SAM from \hbar to $-\hbar$ (or *vice versa*), converting the momentum into the OAM. The obtained mixture of the left- and right-circularly polarized light then goes through another set of a quarter wave plate and a polarizer to eliminate the untransformed light for the CCD detection of the optical vortex.

The pictures in Fig. 7(a) of the obtained optical vortex beams from the green ($\lambda = 532$ nm) and red ($\lambda = 638$ nm) laser sources demonstrate the donut shape with the singularity in the center. As seen in Fig. 7(b), the interference pattern of the

vortex beam with an opposite handed L/R-CP polarized light has the OAM with $l = +2$ and -2 . Meanwhile, with linearly polarized incident light, which can be considered as an equal combination of L- and R-CP, the output in Fig. 7(c) has a combination of two vortex beams with R- and L-CP. The pattern in Fig. 7(c) can be measured with the setup in Fig. 6(a) with both the QWP removed. This can be described as shown in Fig. 7(d) on an OAM Poincaré sphere as the combination of two vortex beams with equal intensity and opposite OAM.

In the same way, Fig. 6(b) illustrates the setup combining an Olympus BX-51 microscope and an optical fiber spectrometer to measure the SOC efficiency over the visible spectrum. In the transmission mode of the microscope, the white light goes through a polarizer and a broad-wavelength-range quarter wave plate to get a circularly polarized incident light onto the metasurface sample. With another set of a quarter-wave plate and a polarizer to filter the untransformed light, the intensity of the remaining output optical vortex is measured with an optical fiber spectrometer. Due to the limitation of the spectrometer and the achromatic wave plates, the SOC efficiency measurement was carried out for the visible spectrum covering the wavelengths from 450 nm to 750 nm. Fig. 7(e) depicts the comparison between the SOC efficiencies of the simulation and experimental results. The two results demonstrate similar trends of the efficiency change over the visible spectrum, where the experimental results cover a broad wavelength range from 565 nm to 715 nm, in which the efficiency over 20% with the highest of 24% at 670 nm is characterized. The efficiency difference between measurements and simulations can be the result of inevitable surface roughness and line-edge roughness of the antenna arms during our nanofabrication process, in combination with the alignment error between the wave plates and polarizers during the optical measurements.

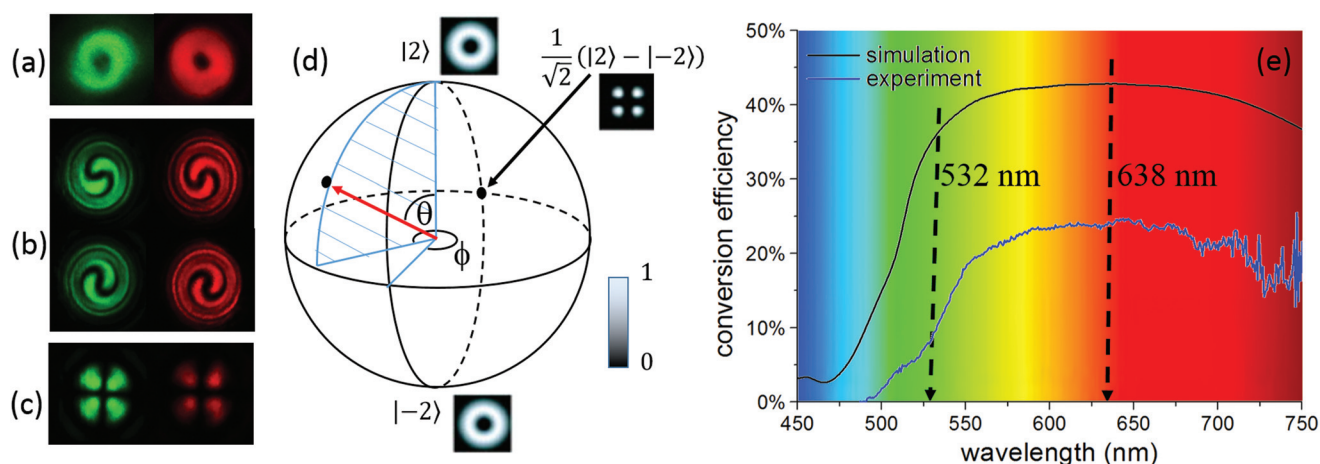


Fig. 7 The measured results of the converted optical vortex by the plasmonic metasurface. (a) The intensity distribution of the converted optical vortex with a donut shape at the wavelengths of 532 nm and 638 nm, respectively. (b) The interference pattern of the transformed beam with an opposite handed circularly polarized light, with the OAM of $l = +2$ and -2 . (c) The interference pattern of two optical vortices with the OAM of $l = +2$ and -2 . (d) The OAM Poincaré sphere description of (a) and (c). (e) A comparison of the efficiency spectra between the simulation and experimental results at the visible frequencies. 532 nm and 638 nm are the wavelengths of the two laser sources used in the setup in Fig. 6(a).

Conclusions

This paper tackles the low efficiency issue of converting a Gaussian beam into a vortex beam in visible light by a plasmonic metasurface with L-shaped Al nano-antennas arranged in concentric circles. A theoretical study using both the Jones matrices and the finite difference time domain method reveals the close relationship between the conversion efficiency and the antenna nature, enabling us to redesign the metasurface with the optimized parameters such as the material, the thickness and the density of the elements in order to maximize the efficiency. State-of-the-art electron beam lithography together with detailed proximity correction including PEC and PPC is applied for the fabrication of the designed metasurface. With the reconstructed metasurface, the converted beams with high quality are demonstrated by optical interference. Quantitative characterization shows a significantly enhanced efficiency up to 20% in the broad wavelength range of 565–715 nm. Compared to the theoretical limit as calculated in this work, 40% at the wavelengths of 548–725 nm for the spin-to-orbit momentum conversation efficiency, there is still room for further improvement. Nevertheless, this work has made a promising step toward high quality plasmonic metasurfaces for applications in quantum optics, communication encryption, optical microscopy and optical tweezers.

Conflicts of interest

There are no conflicts to declare.

Acknowledgements

This project is supported by the Natural Science Foundation of Shanghai (Grant no. 16ZR1445900 and 16JC1403100), the STCSM (Grant no. 15JC1401000) and the National Natural Science Foundation of China (Grant no. 61574043 and 11734007).

Notes and references

- L. J. Allen, M. W. Beijersbergen, R. J. C. Spreeuw and J. P. Woerdman, *Phys. Rev. A*, 1992, **45**, 8185–8189.
- L. Marrucci, E. Karimi, S. Slussarenko, B. Piccirillo, E. Santamato, E. Nagali and F. Sciarrino, *J. Opt.*, 2011, **13**, 064001.
- N. Yu and F. Capasso, *Nat. Mater.*, 2014, **13**, 139–150.
- A. Mair, A. Vaziri, G. Weihs and A. Zeilinger, *Nature*, 2001, **412**, 313–316.
- E. Karimi, S. A. Schulz, I. De Leon, H. Qassim, J. Upham and R. W. Boyd, *Light: Sci. Appl.*, 2014, **3**, e167.
- J. Wang, J. Yang, I. M. Fazal, N. Ahmed, Y. Yan, H. Huang, Y. Ren, Y. Yue, S. Dolinar and M. Tur, *Nat. Photonics*, 2012, **6**, 488–496.
- N. Bozinovic, Y. Yue, Y. Ren, M. Tur, P. Kristensen, H. Huang, A. E. Willner and S. Ramachandran, *Science*, 2013, **340**, 1545–1548.
- D. Zhang, X. Feng and Y. Huang, *Opt. Express*, 2012, **20**, 26986–26995.
- G. C. G. Berkhout, M. P. J. Lavery, J. Courtial, M. W. Beijersbergen and M. J. Padgett, *Phys. Rev. Lett.*, 2010, **105**, 153601.
- A. T. Oneil, I. Macvicar, L. J. Allen and M. J. Padgett, *Phys. Rev. Lett.*, 2002, **88**, 053601.
- A. M. Yao and M. J. Padgett, *Adv. Opt. Photonics*, 2011, **3**, 161–204.
- G. Vallone, V. D'Ambrosio, A. Sponselli, S. Slussarenko, L. Marrucci, F. Sciarrino and P. Villoresi, *Phys. Rev. Lett.*, 2014, **113**, 060503.
- Z. Zhou, Y. Li, D. Ding, W. Zhang, S. Shi, B. Shi and G. Guo, *Light: Sci. Appl.*, 2014, **5**, e16019.
- V. Dambrosio, N. Spagnolo, L. D. Re, S. Slussarenko, Y. Li, L. C. Kwek, L. Marrucci, S. P. Walborn, L. Aolita and F. Sciarrino, *Nat. Commun.*, 2013, **4**, 2432–2432.
- A. Nicolas, L. Veissier, L. Giner, E. Giacobino, D. Maxein and J. Laurat, *Nat. Photonics*, 2014, **8**, 234–238.
- C. Zhang, C. Min, L. Du and X.-C. Yuan, *Appl. Phys. Lett.*, 2016, **108**, 201601.
- P. G. Lu Yan, E. Karimi, A. Rubano, L. Marrucci, R. W. Boyd and S. Ramachandran, *Optica*, 2015, **2**, 900–903.
- M. Gecevičius, R. Drevinskis, M. Beresna and P. G. Kazansky, *Appl. Phys. Lett.*, 2014, **104**, 231110.
- K. Volksepulveda, S. Chavezcerda, V. Garceschavez and K. Dholakia, *J. Opt. Soc. Am. B*, 2004, **21**, 1749–1757.
- G. Foo, D. M. Palacios and G. A. Swartzlander, *Opt. Lett.*, 2005, **30**, 3308–3310.
- E. Mari, F. Tamburini, G. Swartzlander, A. Bianchini, C. Barbieri, F. Romanato and B. Thidé, *Opt. Express*, 2012, **20**, 2445–2451.
- M. W. Beijersbergen, R. P. C. Coerwinkel, M. Kristensen and J. P. Woerdman, *Opt. Commun.*, 1994, **112**, 321–327.
- W. Lee, X.-C. Yuan and W. Cheong, *Opt. Lett.*, 2004, **29**, 1796–1798.
- V. Kotlyar, A. Kovalev, V. Soifer, C. S. Tuvey and J. A. Davis, *Opt. Lett.*, 2007, **32**, 921–923.
- C. Gao, X. Qi, Y. Liu, J. Xin and L. Wang, *Opt. Commun.*, 2011, **284**, 48–51.
- N. Gonzalez, G. Molinaterriza and J. P. Torres, *Opt. Express*, 2006, **14**, 9093–9102.
- I. V. Basistiy, V. Y. Bazhenov, M. S. Soskin and M. V. Vasnetsov, *Opt. Commun.*, 1993, **103**, 422–428.
- N. Heckenberg, R. McDuff, C. Smith and A. White, *Opt. Lett.*, 1992, **17**, 221–223.
- D. Mawet, E. Serabyn, K. Liewer, C. Hanot, S. McEldowney, D. Schemo and N. O'Brien, *Opt. Express*, 2009, **17**, 1902–1918.
- M. P. J. Lavery, A. Dudley, A. Forbes, J. Courtial and M. J. Padgett, *New J. Phys.*, 2011, **13**, 093014.
- J. Leach, M. J. Padgett, S. M. Barnett, S. Frankearnold and J. Courtial, *Phys. Rev. Lett.*, 2002, **88**, 257901.

- 32 C.-W. Qiu and Y. Yang, *Science*, 2017, **357**, 645–645.
- 33 Y. Yang, W. Wang, P. Moitra, I. I. Kravchenko, D. P. Briggs and J. Valentine, *Nano Lett.*, 2014, **14**, 1394–1399.
- 34 Y. Zhao and A. Alù, *Phys. Rev. B: Condens. Matter Mater. Phys.*, 2011, **84**, 205428.
- 35 M. I. Shalaev, J. Sun, A. Tsukernik, A. Pandey, K. Nikolskiy and N. M. Litchinitser, *Nano Lett.*, 2015, **15**, 6261–6266.
- 36 D. Hakobyan, H. Magallanes, G. Seniutinas, S. Juodkazis and E. Brasselet, *Adv. Opt. Mater.*, 2016, **4**, 306–312.
- 37 D. Lin, P. Fan, E. Hasman and M. L. Brongersma, *science*, 2014, **345**, 298–302.
- 38 X. Ma, M. Pu, X. Li, C. Huang, Y. Wang, W. Pan, B. Zhao, J. Cui, C. Wang and Z. Zhao, *Scientific Reports*, 2015, **5**, 10365–10365.
- 39 G. X. Li, M. Kang, S. Chen, S. Zhang, E. Y. B. Pun, K. W. Cheah and J. Li, *Nano Lett.*, 2013, **13**, 4148–4151.
- 40 F. Qin, L. Ding, L. Zhang, F. Monticone, C. C. Chum, J. Deng, S. Mei, Y. Li, J. Teng, M. Hong, S. Zhang, A. Alù and C.-W. Qiu, *Sci. Adv.*, 2016, **2**, e1501168.
- 41 F. Yue, D. Wen, J. Xin, B. D. Gerardot, J. Li and X. Chen, *ACS Photonics*, 2016, **3**, 1558–1563.
- 42 M. Khorasaninejad, W. Chen, R. C. Devlin, J. Oh, A. Y. Zhu and F. Capasso, *Science*, 2016, **352**, 1190–1194.
- 43 M. Q. Mehmood, S. Mei, S. Hussain, K. Huang, S. Y. Siew, L. Zhang, T. Zhang, X. Ling, H. Liu, J. Teng, A. Danner, S. Zhang and C.-W. Qiu, *Adv. Mater.*, 2016, **28**, 2533–2539.
- 44 F. Bouchard, I. De Leon, S. A. Schulz, J. Upham, E. Karimi and R. W. Boyd, *Appl. Phys. Lett.*, 2014, **105**, 101905.
- 45 J. Jin, J. Luo, X. Zhang, H. Gao, X. Li, M. Pu, P. Gao, Z. Zhao and X. Luo, *Scientific Reports*, 2016, **6**, 24286.
- 46 N. Yu, P. Genevet, M. A. Kats, F. Aieta, J. Tetienne, F. Capasso and Z. Gaburro, *Science*, 2011, **334**, 333–337.
- 47 X. Ling, X. Zhou, X. Yi, W. Shu, Y. Liu, S. Chen, H. Luo, S. Wen and D. Fan, *Light: Sci. Appl.*, 2015, **4**, e290.
- 48 Y. Liu, X. Ling, X. Yi, X. Zhou, H. Luo and S. Wen, *Appl. Phys. Lett.*, 2014, **104**, 191110.
- 49 Z. Liu, Y. Liu, Y. Ke, Y. Liu, W. Shu, H. Luo and S. Wen, *Photonics Res.*, 2017, **5**, 15–21.
- 50 N. Yu, P. Genevet, F. Aieta, M. A. Kats, R. Blanchard, G. Aoust, J.-P. Tetienne, Z. Gaburro and F. Capasso, *IEEE J. Sel. Top. Quantum Electron.*, 2013, **19**, 4700423–4700423.
- 51 S. Mei, M. Q. Mehmood, S. Hussain, K. Huang, X. Ling, S. Y. Siew, H. Liu, J. Teng, A. Danner and C. W. Qiu, *Adv. Funct. Mater.*, 2016, **26**, 5255–5262.
- 52 W. Luo, S. Xiao, Q. He, S. Sun and L. Zhou, *Adv. Opt. Mater.*, 2015, **3**, 1102–1108.
- 53 W. Luo, S. Sun, H.-X. Xu, Q. He and L. Zhou, *Phys. Rev. Appl.*, 2017, **7**, 044033.
- 54 Y. Chen, *Microelectron. Eng.*, 2015, **135**, 57–72.